Journal of Instrumentation

PAPER • **OPEN ACCESS**

Commissioning the digital mass-filter/ion-trap module for the MS SPIDOC prototype

To cite this article: Florian Simke *et al* 2023 *JINST* **18** P10021

Published by IOP Publishing for Sissa Medialab

Received: *July 17, 2023*
Accepted: *August 30, 2023*
Published: *October 18, 2023*

Commissioning the digital mass-filter/ion-trap module for the MS SPIDOC prototype

Florian Simke,[a,*] **Paul Fischer,**[a] **Tomislav Damjanović,**[b,c,d,e] **Alan Kádek,**[b,c,f] **Thomas Kierspel,**[b,d] **Kristina Lorenzen,**[c] **Charlotte Uetrecht**[b,d,e] **and Lutz Schweikhard**[a]

[a] *Institut für Physik, Universität Greifswald,*
Felix-Hausdorff-Str. 6, 17489, Greifswald, Germany
[b] *Leibniz Institute of Virology (LIV),*
Martinistraße 52, 20251, Hamburg, Germany
[c] *European XFEL,*
Holzkoppel 4, 22869, Schenefeld, Germany
[d] *Centre for Structural Systems Biology (CSSB), Deutsches Elektronen-Synchrotron DESY,*
Notkestraße 85, 22607, Hamburg, Germany
[e] *Faculty V: School of Life Sciences, University of Siegen,*
Adolf-Reichwein-Str. 2a, 57076, Siegen, Germany
[f] *Institute of Microbiology (BIOCEV), Czech Academy of Sciences,*
Prumyslova 595, 25250, Vestec, Czech Republic

E-mail: florian.simke@uni-greifswald.de

2023 JINST 18 P10021

Abstract: The combination of a linear quadrupole ion-filter and linear Paul trap operated with a rectangular guiding field for the filtering and accumulation of ions within the **M**ass **S**pectrometry for **S**ingle **P**article **I**maging of **D**ipole **O**riented protein **C**omplexes (MS SPIDOC) prototype [T. Kierspel et al., *Anal. Bioanal. Chem.*, published online] is characterized. Using cationic caesium-iodide clusters, the ion-separation performance, ion accumulation, cooling, and ejection via in-trap pin electrodes is evaluated. Furthermore, proof-of-principle measurements are performed with 64 kDa multiply-charged non-covalent protein complexes of human hemoglobin and 804 kDa non-covalent complex of GroEL, to demonstrate that the module meets the criteria to handle high-mass ions which are the main objective of the MS SPIDOC project. The setup's performance is found to be in line with previous results from ion-trajectory simulations [F. Simke et al., *Int. J. Mass Spectrom.* **473** (2022) 116779].

Keywords: Mass spectrometers; Instrumentation for radioactive beams (fragmentation devices, fragment and isotope, separators incl. ISOL, isobar separators, ion and atom traps, weak-beam diagnostics, radioactive-beam ion sources); Instrumentation for FEL

---

[*] Corresponding author.

https://doi.org/10.1088/1748-0221/18/10/P10021

Contents

2023 JINST 18 P10021

1 Introduction

The knowledge of the molecular structure of proteins is fundamental for the understanding of biological processes and for the development of new medical treatments [1–3]. The **M**ass **S**pectrometry for **S**ingle **P**article **I**maging of **D**ipole **O**riented protein **C**omplexes (MS SPIDOC) project aims to study mass- and conformation-separated protein complexes via single-particle X-ray diffraction [4–7]. To this end, a sample-delivering prototype has been developed, which aims to provide native protein complexes with a mass m up to the megadalton (MDa) mass range for single-particle-imaging (SPI) experiments at, e.g., the European X-Ray Free-Electron Laser (XFEL) facility [8–10]. Additionally, to simplify the analysis of diffraction patterns obtained from the SPI process, dipole orientation will be used to further control the proteins [11, 12].

The MS SPIDOC prototype consists of a number of individual modules, developed by different partners[1] of the consortium located throughout Europe. After initial tests at the location of each partner, the modules are assembled into the full prototype. In the following, the **D**igital **I**on **T**rap (DIT)-module, built at the University of Greifswald, is characterized with caesium-iodide cations $[(\mathrm{CsI})_n\mathrm{Cs}]^+$ on site, without the other modules attached. The results are compared to computational simulations previously performed for this module [13]. Additional measurements with multiply-charged hemoglobin (Hb^{z+}) and GroEL (GroEL^{z+}) ions in a test setup paired with the upstream ion source and transfer module are performed at the European XFEL facility in Hamburg.

---

[1] https://www.ms-spidoc.eu/partners.

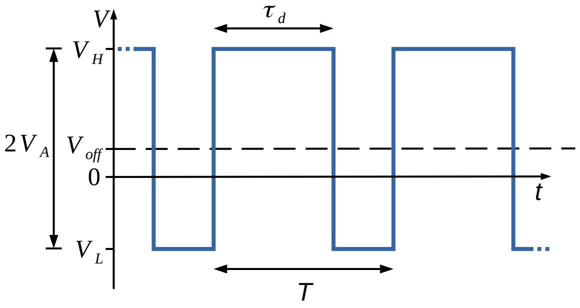

Figure 1. Rectangular (digital) waveform with high and low voltages V_H and V_L, respectively, amplitude V_A, period T, and offset voltage V_off. Reprinted from [13], Copyright (2022), with permission from Elsevier.

2023 JINST 18 P10021

2 Digital guiding-field waveforms

The generation of sinusoidal guiding fields for mass-filters and ion traps can be technically challenging. In contrast, using a rectangular (digital) radio-frequency (RF) waveform has several advantages. In particular, it is possible to quickly change the order of magnitude of the accepted mass-to-charge ratio m/z, where z is the charge state, and to construct an electrical implementation without the need of a resonant circuit. Furthermore, the digital waveform allows the handling of ions with higher m/z, i.e. heavy biomolecules, at lower rf-amplitudes by reducing the frequency [14, 15]. Note that, in the present study, RF always refers to a digital waveform. This does not significantly change the way mass filters and traps operate compared to a harmonic waveform [16, 17]. After being introduced by Richards in 1973 [18, 19], digital-driven mass-filters and ion traps were not widely used until Ding and Sudakov [20, 21] started to further develop the technique in 2002. Since then, the technique has been used in an increasing number of applications [22–27].

A digital waveform (figure 1) is characterized by a frequency f, amplitude

$$V_\mathrm{A} = \frac{V_\mathrm{H} - V_\mathrm{L}}{2} \tag{2.1}$$

where V_H is the higher voltage and V_L is the lower voltage, and a duty cycle

$$d = \frac{\tau_\mathrm{d}}{T} \tag{2.2}$$

where $T = 1/f$ is the full period and τ_d the part during which V_H is applied. The common offset voltage with respect to ground potential is then given by

$$V_\mathrm{off} = \frac{V_\mathrm{H} + V_\mathrm{L}}{2}\,. \tag{2.3}$$

In a digital-operated quadrupole mass filter (QMF) the conditions for stable trajectories of charged particles are obtained by solving the Hill-equation [18, 28, 29] for the given geometry. These conditions as well as the mass-selection principle of a digital QMF are already described in [13]. Briefly, the transmitted mass-to-charge follows $m/z \propto 1/f^2$. The duty cycle determines the width of the transmitted m/z-range, where $d = 50\,\%$ gives the widest and $d \approx 61.2\,\%$ [23] the smallest possible range. For a frequency scan, the mass-resolving power

$$R = \frac{f}{2\Delta f}, \tag{2.4}$$

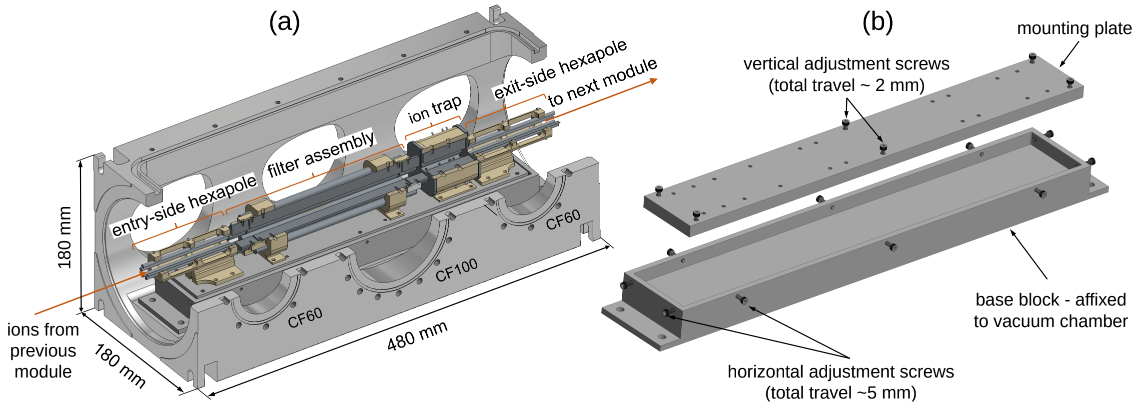

Figure 2. (a) Model of the DIT module. Ions from the previous module are guided through the entry-side hexapole, mass selected in the filter assembly, accumulated and bunched in the ion trap, and ejected via the exit-side hexapole into the next module. (b) Base block and mounting plate with threaded holes for horizontal and vertical alignment of the module.

where Δf is the full width at half maximum (FWHM) of a signal in the frequency spectrum, depends on the selected duty cycle. As described in detail in section 3.3, a signal in a frequency spectrum is obtained by evaluating the number of ions which are transmitted for a given frequency of the filter.

3 Experimental setup

One of the design goals of the MS SPIDOC prototype is to create a flexible device for ion delivery and ion-photon interaction studies at different XFEL or synchrotron facilities. To that end, the individual modules can be reordered or removed without affecting the functionality of the others. Generally, however, the setup configuration obeys the following principle: ion source and transfer into high vacuum region, ion preparation, interaction, and detection (for more details, see [6]).

To guarantee technical compatibility, all partners use the same, customized design for the vacuum chamber. Additionally, the same hexapole guiding elements are employed at each module's entry and exit to facilitate ion transfer between the modules. This will be described in more detail in an upcoming publication about the full prototype. The hexapoles of the DIT module are operated with a digital waveform with 50 % duty cycle and 500 kHz (table 1). They transmit ions of a broad mass range from the entry side of the module to the filter and from the trap to the exit side.

3.1 Overview and mounting

A detailed overview of the DIT module is given in [13]. Briefly, the module (figure 2a) receives an ion beam (continuous or pulsed) from the previous module through an aperture (not shown) and the entry-side hexapole. A quadrupole-mass-filter assembly composed of two short and one long segments selects ions from the incoming beam according to their m/z. With a linear Paul trap, the ions are accumulated, thermalized, and released as a well-defined bunch. As mentioned in detail in [13], the module has to be able to provide mass-selected biomolecules of several thousand to tens of thousands of Thomson with a mass resolution ideally higher than $R = 100$. Additionally, the temporal width of the outgoing ion bunch has to be less than 100 µs for subsequent conformation

Table 1. Amplitude V_A, frequency f, duty cycle d, and offset V_off of the RF-waveforms applied to the module components. Values denoted with * are changed depending on transmitted mass range. The hexapole V_off values denote the entry side (no brackets) and exit side (brackets), respectively.

component	V_A/ V	f/ kHz	d/ %	V_off/ V
hexapole	100	500	50	0 (−10)
filter	200	350^*	50 . . . 61	0
trap	175	350^*	50	−3

Table 2. Upper and lower DC voltages $V_\mathrm{DC,u}$ and $V_\mathrm{DC,l}$ for endcaps and in-trap pins.

component	$V_\mathrm{DC,u}$ / V	$V_\mathrm{DC,l}$ / V
entry-endcap	50	5
pin row 1	250	−3
pin row 2	200	−30
pin row 3	100	−80
exit-endcap	50	−10

separation and has to have a high density to increase the probability of X-ray interactions at a beamline of the European XFEL facility.

The components of the DIT module are mounted on a rigid mounting plate. The plate itself is embedded into a base block and held in place with adjustment screws (figure 2b). Changing the depth of the ten horizontal and six vertical screws allows fine tuning of the alignment with other modules in all three dimensions.

For the application of buffer gas (here nitrogen, but later also argon or xenon), the encapsulated trap is connected to a gas inlet and pumped via the endcap openings. This couples the trap pressure to the main chamber pressure which is pumped by a turbomolecular pump (Pfeiffer, HiPace 400). Since the pressure in the trap is not measured directly, the pressure inside the gas-inlet is used as an upper-bound estimate and the pressure inside the main chamber as a lower-bound estimate. The gas inlet (not shown in figure 2) consists of a gas reservoir and an automatic regulating valve with control unit (Pfeiffer, EVR 116 and RVC 300) connected to the exit-side CF60 port. To prevent damage due to electric sparks, the pressure in the main chamber is limited to $\approx 10^{-4}$ hPa, corresponding to a pressure of ≈ 1 hPa in the gas inlet.

The operating RF waveform of each component is generated independently by sets of two power supplies providing V_H and V_L (FUG, MCP 350–1250 or 700–1250), a fast high-voltage (HV) switch (CGC, AMX1500-3E), and a frequency generator (Keysight, 33522B) providing control signals for the switch. All RF generators of the same frequency are coupled to ensure phase synchronicity. Typical RF parameters are shown in table 1. The duty cycle is varied between 50 % and ca. 61 % at the longer filter rods only, the shorter parts are operated at 50 % to aid the ion transition across field boundaries. To control experimental timings and data acquisition, an in-house control software based on LabVIEW [30] and a Field-Programmable-Gate-Array (FPGA) card (National Instruments, PCI-7811R) is used. The FPGA card generates transistor-transistor logic (TTL) pulses which can be processed by all devices of the setup parts attached to the module.

3.2 Trap operation

The linear Paul trap (figure 3 top) consists of two endcaps with aperture diameters of 6 mm and 4 mm on the entry and exit side, respectively, four quadrupole rods, and three rows of four pins located between the rods. The timing pattern of the experimental cycle is shown in figure 4. The ions enter the

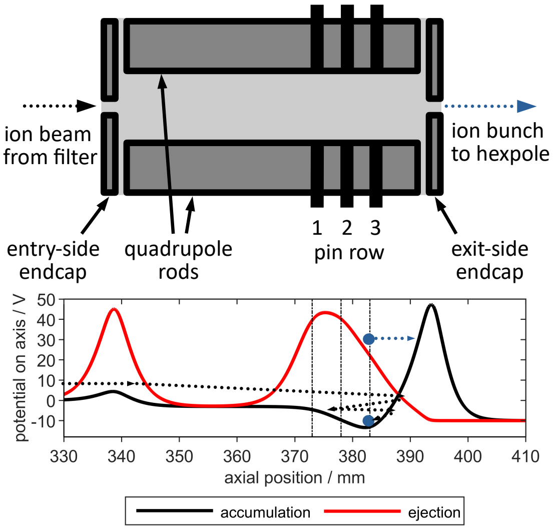

Figure 3. Schematic overview of the encapsulated trap (top) and calculated axial potential (bottom) for accumulation and ejection. Values from table 2 are used for calculation. The dotted lines indicate the operation principle. Origin of axial-position axis same as figure 4 in [13]).

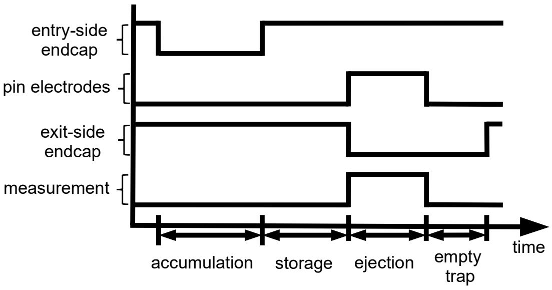

Figure 4. Signal logic of an experimental cycle to accumulate and bunch an incoming continuous ion beam.

trap with an axial kinetic energy slightly above the potential of the entry-side endcap (dotted black line, figure 3 bottom). During the accumulation time (solid black line), the potential barrier of the exit-side endcap reflects the ions. If they lose enough axial-kinetic energy due to background-gas collisions within one circulation in the trap, they are reflected by the potential of the entry-side endcap. In this case they are captured and cooled into the potential minimum formed by the pin rows. Otherwise they leave the trap. After a storage time (t_s), during which the entry-side endcap is switched up to block incoming ions, the pin and exit-side-endcap potentials are switched to eject the ions (red line, figure 3 bottom). After ejection, all potentials save for the entry-side endcap are switched to their low states for several milliseconds to purge the trap of any remaining ions. The applied voltages for the upper ($V_{\mathrm{DC,u}}$) and lower ($V_{\mathrm{DC,l}}$) potential states of the components, provided by a 12-channel power supply (Iseg, EBS C005) are shown in table 2. These values result from an iterative optimization process. The resulting ion bunch characteristics for this axial configuration are given in section 4.3.

There are two differences between the present module and the one for which simulation results are given in [13]. The present trap has three pin rows instead of two to better shape the axial potential. Furthermore, in contrast to the simulation, the reduced axial potential in front of the trap is not applied (compare figure 3 here to figure 4 in [13]). Experiments show that the use of the potential well actually decreases the signal intensity in the present setup. Nevertheless, if necessary, a negative potential could be easily applied in future cases.

3.3 Detector calibration

A MagneTOF MINI (ETP Ion Detect, 14DM497) is used for ion detection for the systematic characterization with CsI and Hb. It is able to record incoming signals from single ions up to

2023 JINST 18 P10021

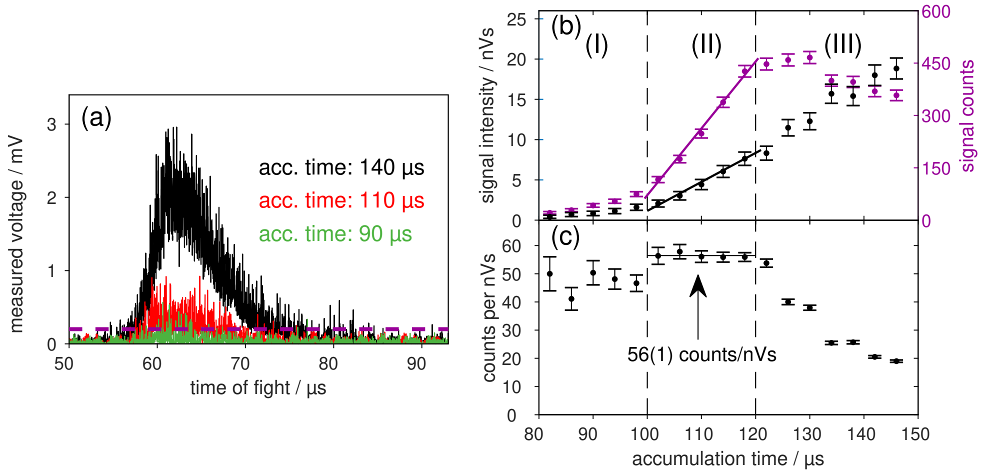

Figure 5. (a) Transients for three different trap accumulation times. The purple dashed line shows the threshold level at which a signal is counted for the accumulation time of 90 µs (b) Integrated transient (signal intensity, black) and discriminated ion counts (purple) as a function of accumulation time. (c) Ratio between signal counts and signal intensity.

continuous currents with a nearly linear response, which is required for the present study. Since the noise level is low enough and the MagneTOF detector provides sufficiently high signals for ion counting, no additional amplifier is necessary. The entrance of the detector is placed about ten millimeters behind the exit of the last hexapole. The output signal is recorded via a Picoscope oscilloscope (Pico Technology, 5442D MSO), yielding a voltage transient (figure 5a). This voltage transient is inverted to get positive values for more intuitive data evaluation and presentation.

To obtain the signal intensity for large ion bunches, the transient is evaluated in two ways simultaneously. In the first evaluation, the signal peaks above a threshold level are counted. It is placed 1 µV above the noise level of the transient (purple dashed line in figure 5a). In the second evaluation, a charge-measurement technique is used: by integrating the transient, a voltage-times-time value (here in nVs) corresponding to the amount of impinged ions is received.

To calibrate the signal intensity to a single ion impact, the amount of ions within the bunch is varied via the trap accumulation time (figure 5a). Here, the filter is set to $f = 389\,\text{kHz}$ and $d = 60.2\%$ to only let $[(\mathrm{CsI})_3\mathrm{Cs}]^+$ enter the trap. Comparing the signal intensity and signal counts reveals three regimes (figure 5b). For the present case, for $T_{\mathrm{acc}} \leq 100\,\mu\mathrm{s}$ (I) the signal-to-noise ratio is too low for reasonable results from the integral method, leading to an overestimation of the signal intensity. For $T_{\mathrm{acc}} \geq 120\,\mu\mathrm{s}$ (III) the amount of ions is too high for single-ion-counting, since the baseline of the transient is rising due to overlap of multiple ion signals in time. This leads, for a fixed threshold, to an underestimation of the signal count rate. For $100\,\mu\mathrm{s} \leq T_{\mathrm{acc}} \leq 120\,\mu\mathrm{s}$, both evaluation methods are viable because their signals increase linearly. Calculating the fixed ratio between the methods (figure 5c) results in the calibration value of 56(1) counts per nVs.

For intensities higher than 200 nVs, the transients start to become asymmetrical. We assume this is a saturation effect from the detector system. However, this does not affect the present measurements except for those shown in figure 10, since their signal intensities are below this threshold.

4 Experimental results

For $[(\mathrm{CsI})_n\mathrm{Cs}]^+$ measurements, performed at the University of Greifswald, a commercial microflow Z-geometry Electro-Spray-Ionization (ESI) [31, 32] source (Micromass/Waters, modified by MS Vision) [33, 34] followed by a short harmonically driven transfer hexapole was coupled onto the entry-side hexapole of the DIT module. A CsI solution of 19 mM in a solvent of 50/50 water/isopropanol is injected from a syringe with a flow rate between 2.5 and 3.7 µl/min.

For testing of high-mass non-covalent protein complexes (i.e. Hb and GroEL) at the European XFEL facility, the module is mounted together with an upstream Ion-Transfer-Interface (ITI) module [35] of the MS SPIDOC prototype [6, 7] preceded by a static nanoESI source [36]. The 10 µM is buffer exchanged into 100 mM ammonium acetate (pH 8.0, Sigma-Aldrich, 99.999% trace metals basis) by two cycles of Micro BioSpin P-6 gel filtration (Bio-Rad). It is sprayed from in-house prepared gold-coated borosilicate glass capillaries (1B120F-4, World Precision Instruments), prepared essentially as described in [37, 38].

To quickly record high-resolution spectra for the proof-of-principle measurements with GroEL, the MagneTOF detector is replaced with a high-mass modified quadrupole time-of-flight (Q-TOF) Ultima (Micromass / MSVision) [39]. The Q-TOF Ultima is a commercially available mass spectrometer comprising an ESI source, an analyzer chamber with a quadrupole mass filter and collision cell, and an orthogonal time-of-flight mass analyzer. In standard operation, the sample is softly ionized using the ESI source and transported into vacuum to the analyzer chamber. The ions can be mass-selected and/or fragmented via collision-induced dissociation before their m/z is measured with the TOF analyzer. For the presented experiments, the setup of nanoESI source, ITI, and DIT module replace the front-end ion optics of the Q-TOF up to the selecting quadrupole. The Q-TOF quadrupole is operated in a broad transmission mode (sinusoidal sweeping of set mass), while the collision cell is operated without applied collision gas ($4 \cdot 10^{-4}$ hPa) and 4 V voltage potential to maximize ion transmission. The mentioned Labview-based control software records the ion signal received from the mass analyzer's multi-channel-plate detector. The 1 µM (14-mer) GroEL was repurified by reassembly and buffer exchanged as described in [40].

During all following measurements, the ions are stored in the trap. To ensure identical trapping conditions while scanning the QMF frequency, the frequency of the trap is coupled to it. If not mentioned otherwise, ions are accumulated for 50 ms and further stored for 10 ms at a gas-inlet pressure of $8.5 \cdot 10^{-1}$ hPa.

4.1 Ion separation

The filter-assembly is used to select specific species from the incoming continuous beam of $[(\mathrm{CsI})_n\mathrm{Cs}]^+$ or Hb^{z+} ions. Figure 6a shows different cluster species transmitted at different QMF frequencies and duty cycles scaling with $1/f^2$. For higher duty cycles, the peak height in the frequency spectrum of each cluster species reduces while their FWHM narrows. By plotting spectra recorded for different duty cycles as a color-coded map, a two-dimensional mass-spectrum is obtained (figure 6b). Each species appears as a triangular structure with narrowing width toward higher duty cycles. Singly charged $[(\mathrm{CsI})_n\mathrm{Cs}]^+$ clusters up to $n = 9$ and doubly charged $[(\mathrm{CsI})_n\mathrm{Cs}_2]^{2+}$ clusters for $n = 7$ to 15 are observed. Compared to the calculated edges of the stable region in (d,f)-space (section 2 in [13]) of each cluster (black lines), the measured regions of stability are inside the

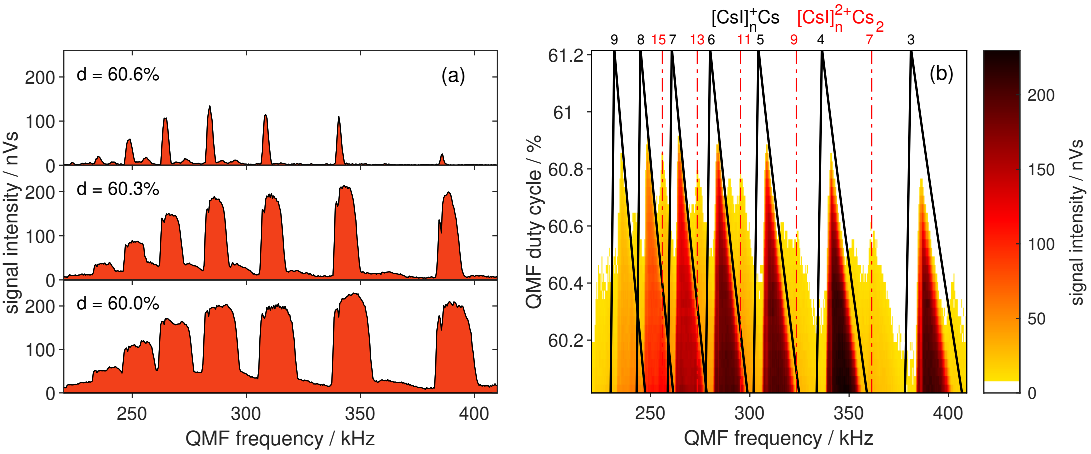

Figure 6. (a) Frequency mass-spectra obtained by horizontal cuts from (b) for three duty cycles.(b) Regions of filter-transmission for $[(CsI)_nCs]^+$ ($n = 3 \ldots 9$) for various duty cycles and frequencies. The black lines are the calculated QMF stability boundaries for the corresponding ions.

calculated ones but do not fill them completely. Deviations from the ideal rise and fall flanks of a rectangular waveform can result in non-stable ion trajectories near the theoretical limits which might explain this reduced area of stability. The discrepancy between the calculated and measured stability region is more prominent for higher frequencies, i.e. lower m/z, which supports the above assumption since RF flanks have a larger impact at shorter periods.

Figure 7 shows the height (red dots) and obtained mass resolving power (blue dots) of the $[(CsI)_5Cs]^+$ signal in the frequency spectrum as a function of duty cycle. For $d < 60.3$ %, the peak height is fairly constant, which indicates that all ions are passing the filter. Raising the duty cycle further leads to a reduced peak height but higher mass-resolving power. The latter rises sharply when approaching $d \approx 60.85$ % while the simulated resolving power (figure 7, open blue squares) shows this behavior at $d \approx 61.21$ %. Note that this difference should not be interpreted as a performance increase. Rather, it is a shift towards lower duty cycles caused by the discrepancy between the expected and measured stability regions. Thus, the tip of the region, where the mass resolving power is highest, is found at lower d values. For the present results, a maximum of $R = 230(30)$ is found at $d = 60.85$ %.

Identical measurements are performed with hemoglobin with a QMF amplitude of $V_A = 150$ V, accumulation time of 10 ms, and storage time of 30 ms (figure 8). The signals match different charge states of Hb^{z+} ($z = 14, 15, 16, 17$). Although, the peaks are not fully separated at $d \leq 60.6$%, a fit of four Gaussians is well suited to describe the spectra (blue dotted lines). A two-dimensional plot of these spectra with calculated stability boundaries (black lines), is shown in figure 9a. A Hb^{15+} ion with $m \approx 64.5$ kDa is equivalent to a mass over charge value of $m/z \approx 4300$ Th. Compared to simulation results for Hb^{15+} (figure 9b), the position of the stability region is similar. A detailed descrition is given in [13]. Briefly, the simulation is performed with the SIMION ion-optics simulation program [41] by solving the Laplace equation for the geometry of this setup with a finite-difference method. The ion trajectory through the resulting potential is computed through a series of finite steps in time. Note that for biomolecules such as hemoglobin, a single charge state peak comprises different species due to residual water and salts adducts through incomplete

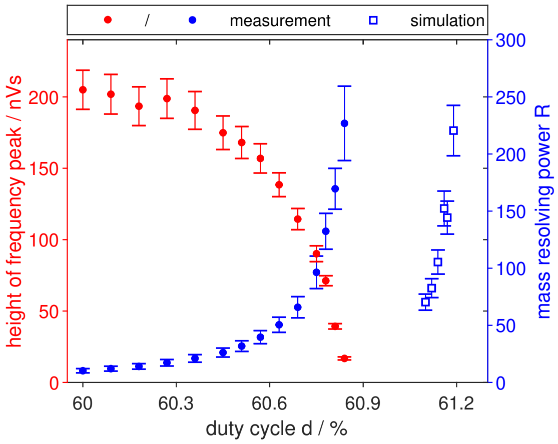

Figure 7. Peak height of the $[(\mathrm{CsI})_5\mathrm{Cs}]^+$ cluster in the frequency spectrum (red dots) and mass resolving power (blue dots) calculated from data of figure 6 as well as simulated (open blue squares taken from [13]).

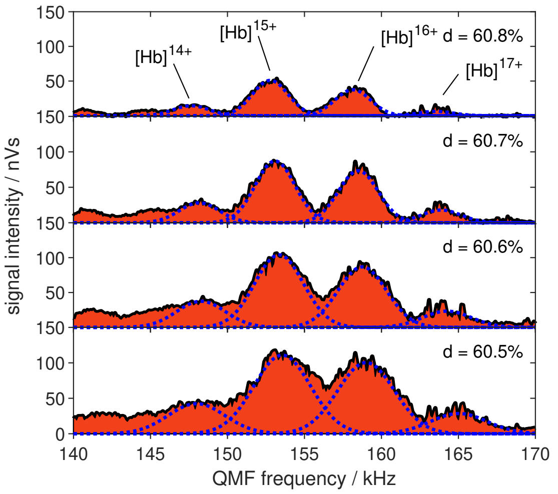

Figure 8. Frequency spectra of Hb^{z+} ions for four duty cycles. The blue dotted lines result from multi-Gaussian fits.

buffer exchange and lower desolvation in gentle native spray. This could be the reason why the measurements fill out the theoretical boundaries of ideal hemoglobin here.

4.2 Ion accumulation and storage

To characterize the loading of ions into the trap, the accumulation time is varied for different gas pressures p (figure 10a). Note that these pressures are measured in the gas inlet, i.e. outside of the trap. For the characterization, $[(\mathrm{CsI})_5\mathrm{Cs}]^+$ is selected in the filter ($f = 311\,\mathrm{kHz}$; $d = 60.2\,\%$). After selection, the ions are stored in the trap for 50 ms. The number of detected ions increases linearly for longer accumulation times. Raising the pressure increases the rate of collisions with the buffer gas, resulting in faster axial-energy loss and, thus, a larger number of ions captured during a given accumulation time. Since the probability of unfolding of heavy biomolecules increases with higher kinetic energy and the amount of collisions with background gas, the pressure of the trap cannot be raised over a certain limit, depending on the ion and background gas species.

Linear fits are made for signal intensities below 200 nVs (see section 3.3). The slopes of the linear fits in figure 10a thus describe the number of accumulated ions per millisecond loading time. As a function of pressure, these values describe the capture efficiency of the trap (figure 10b). It increases steadily for pressures above ≈ 0.1 hPa. Based on the simulations (figure 10 in [13]), a capture efficiency of 100 % is expected above a certain pressure, meaning that the observed ion number should no longer increase. As already discussed above in section 3.1, the pressure can only be increased to a limit of 1 hPa in the present setup, which is not high enough to observe this saturation. Additionally, the MS SPIDOC prototype is expected to handle different proteins in a state as native as possible. This leads to additional constrains regarding the amount of gas in the trap to suppress, e.g., collision-induced unfolding processes of the protein complexes [42, 43]. In practice, the ratio between the trap and chamber pressures can be adjusted by changing the end-cap apertures to suit a given experiment's specific requirements.

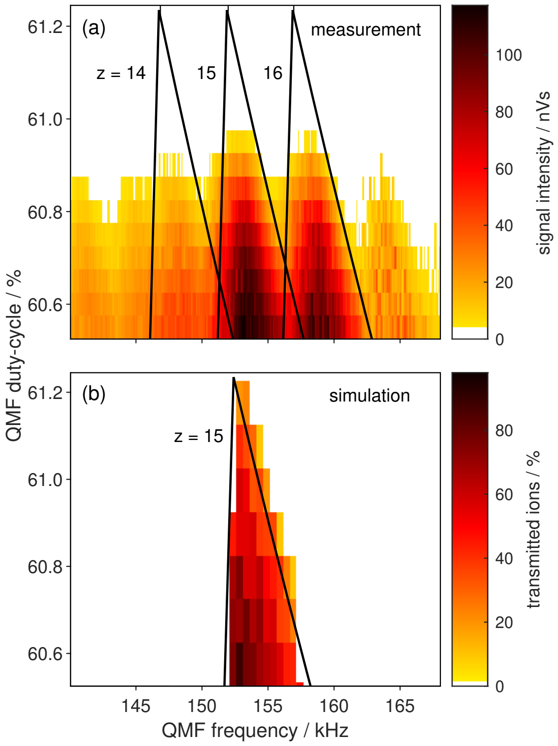

Figure 9. (a) Regions of filter-transmission for Hb^{14+}, Hb^{15+}, and Hb^{16+} for various duty cycles and frequencies. The black lines are the calculated boundaries for the corresponding ions. (b) Results of the simulation for Hb^{15+} [13].

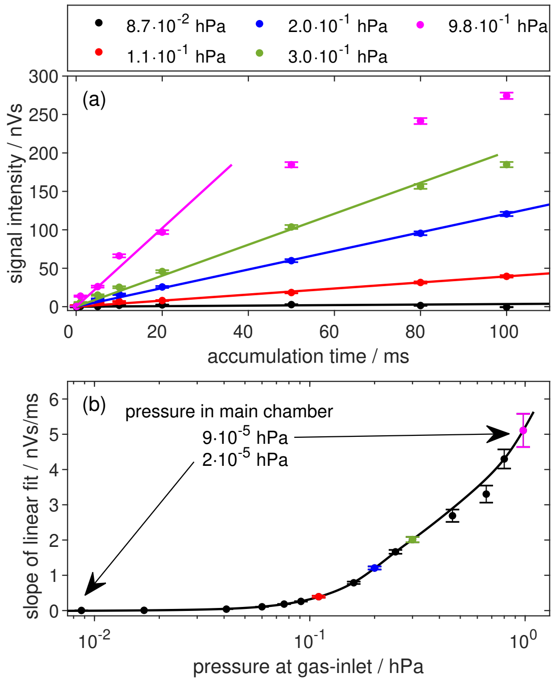

Figure 10. (a) Signal intensity of $[(CsI)_5Cs]^+$ after 50 ms storage time as a function of accumulation time for different buffer-gas pressures. (b) Slope of the linear fit shown in (a) as a function of the gas pressure. The pressure is measured in the gas-inlet system outside the trap. Line is to guide the eye.

By plotting the transients for different storage times in a color-coded map, the process of thermalization is visualized (figure 11). Figure 12 shows the FWHM of Gaussian fits as well as height and signal intensity of the transients from figure 11. Note that the signals deviate from purely Gaussian shapes at lower storage times due to tailing. However, the overall trend of the fitting parameters shown in figure 12 is still representative of the cooling timescales. For the measurement, the pressure is set to $2.5 \cdot 10^{-1}$ hPa and the accumulation time to 500 µs. The latter means that the first ions experience collisional cooling 500 µs longer than the last ones. At low storage times ($<$ 500 µs), the ions are still scattered across the full trap length at the time of ejection. This leads to a portion of the stored ions not being detected after switching to extraction settings. Thus, the signal intensity in figure 12c is at a lower value. At around one millisecond storage time, all ions have started to cool into the potential well formed by the in-trap pins, leading to the signal intensity saturating. They are not yet fully thermalized into the potential minimum since the height of the transients (figure 12b) is still increasing while the FWHM (figure 12a) is decreasing. This process is finished at storage times above two milliseconds for the present parameters. From an exponential fit to the narrowing of the FWHM (red line) a thermalization time $\tau = 0.26(1)$ ms and minimal FWHM of 4(1) µs is obtained for $[(CsI)_5Cs]^+$.

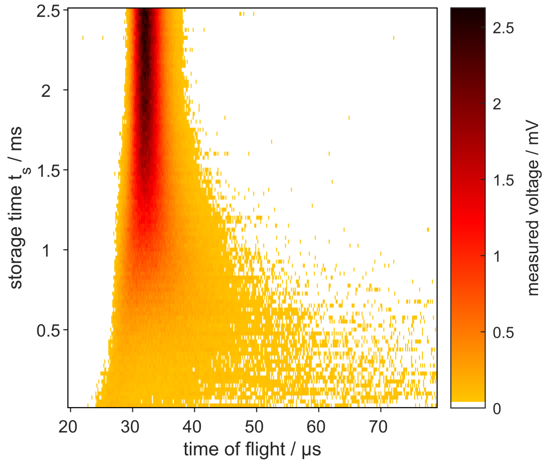

Figure 11. 2D color-coded map of the transients illustrate the thermalization of $[(\mathrm{CsI})_3\mathrm{Cs}]^+$ for 0.5 ms accumulation time and pressure of $2.5 \cdot 10^{-1}$ hPa. Transients after ion ejection are plotted as horizontal lines with increasing storage time on the ordinate.

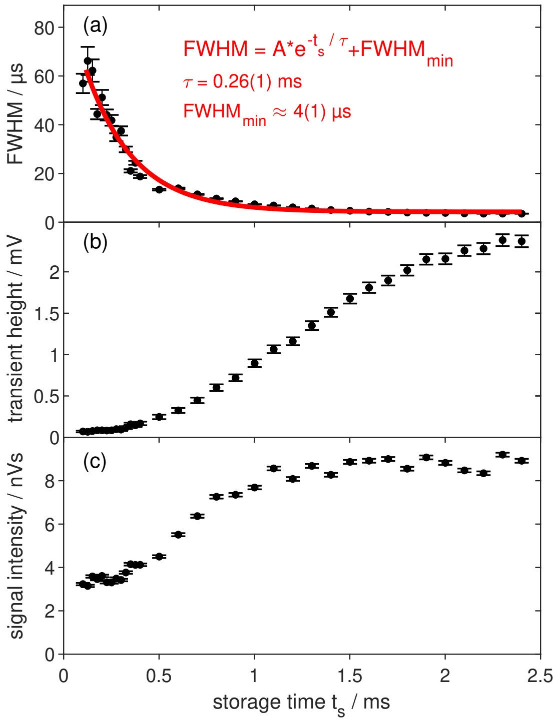

Figure 12. FWHM (a), height of the measured voltage transient (b), and signal intensity (c) as a function of storage time for the spectra shown in figure 11.

Longer storage times are investigated by accumulating $[(\mathrm{CsI})_3\mathrm{Cs}]^+$ ions for 10 ms and storing them for up to 100 ms (figure 13). No losses are observed, confirming that the setup is able to accommodate the projected cycle rates of 10 Hz given by the European XFEL [8]. Additionally, proof-of-principle measurements are performed with GroEL ($m \approx 804$ kDa, $z = 62$) (figure 14). Here, GroEL is accumulated for 10 ms and stored for 5 ms in the trap showing that even ions approaching a MDa in mass can be transmitted through the QMF and are successfully trapped.

4.3 Characterization of ejected ion bunch

Changing the gradient of the ejection potentials affects the outgoing bunch. For the data of figure 15 $[(\mathrm{CsI})_3\mathrm{Cs}]^+$ is accumulated for 35 ms and stored for 50 ms. The voltages applied to pin rows 1 and 3 during the ejection state are varied, with pin row 2 always being adjusted to a value 50 V below row 1. For each combination, the signal intensity (figure 15a) and FWHM (figure 15b) is extracted from a Gaussian fit to the transient. The ions are only ejected when the potential of the exit-side pin-row is lower than that of the entry-side one. An area of high intensity of ca. 200 nVs corresponding to ≈ 10, 000 ions and low FWHM ≈ 10µs is obtained when the entry-side pin is about 100 V higher than the exit side. Edge effects are visible when both pin potentials are nearly identical: some configurations with relatively low FWHM can be found. However, this is a result of a very low signal intensity, which is not a desired mode of operation. Note that, in comparison with

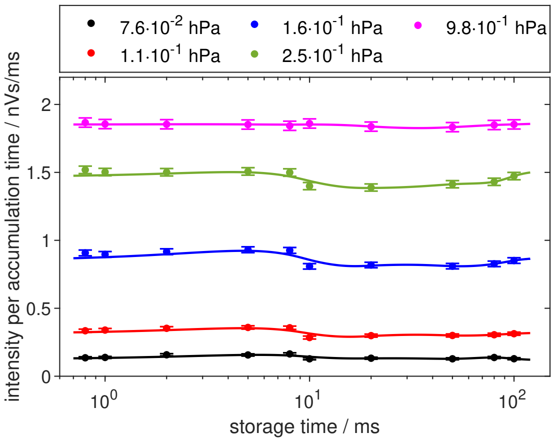

Figure 13. $[(\mathrm{CsI})_3\mathrm{Cs}]^+$ intensity as a function of storage time for different pressures. Lines are added to guide the eye.

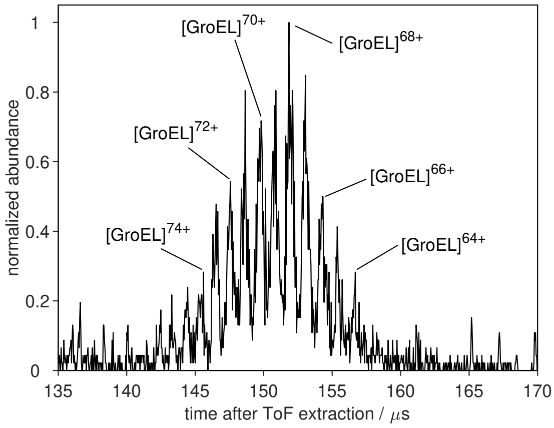

Figure 14. ToF spectra of trapped GroEL^{z+} ($z = 64\ldots74$), using Q-TOF as mass analyser.

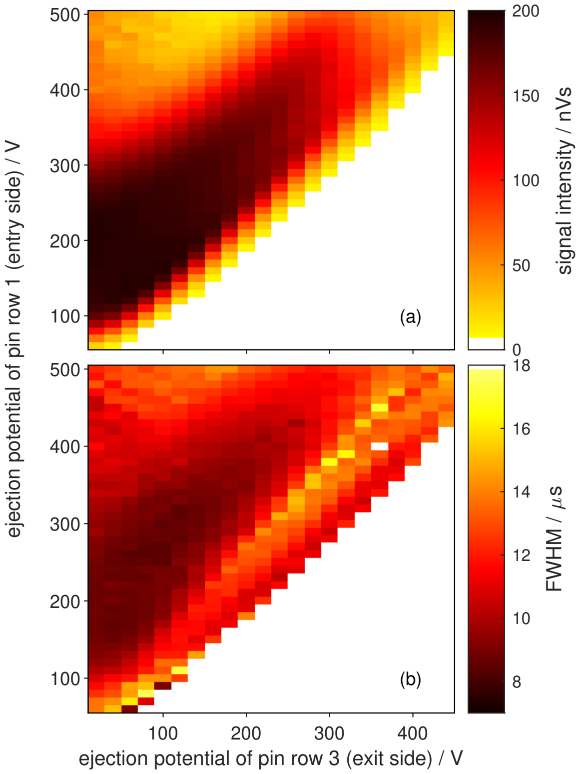

Figure 15. (a) Signal intensity and (b) transient's FWHM of a $[(\mathrm{CsI})_3\mathrm{Cs}]^+$ ion bunch at the end of the exit-side hexapole for different ejection potentials.

figure 12, the minimal FWHM is doubled because the total amount of stored ions is twenty-five times higher. Nevertheless, these FWHM values are sufficiently far below the 100 μs needed for the future time-of-flight conformation separation experiments [13].

5 Summary, conclusion and outlook

First experimental measurements are performed with $[(\mathrm{CsI})_n\mathrm{Cs}]^+$ clusters for the characterization of the digital mass-filter/ion-trap module for the MS SPIDOC prototype. Additionally, mass filtering of non-covalent protein complex Hb^{z+} ions and proof-of-principle measurements of trapping GroEL^{z+} are performed. The results are compared to previous simulations [13]. The present work shows that the module is capable of filtering ions with a mass resolving power up to $R = 230(30)$, which is comparable to the simulation and capable of selecting cluster sizes or biomolecule charge states. The digital ion trap is able to accumulate incoming ions and thermalize them within a few milliseconds. No ion losses are observed up to storage times of a hundred milliseconds, suitable for cycle rates synchronized to the free-electron laser at the European XFEL facility. The temporal width of the ejected ion bunch is optimized through tuning of the in-trap pin potentials to create a high density-bunch with a FWHM on the order of ten mircoseconds at the exit of the module. The DIT module has since been merged with the other modules of the MS SPIDOC prototype at European XFEL, where tests with very large protein assemblies such as multi-MDa particles will be performed, followed by its installation at various beamlines.

Further developments of the DIT module will be performed based on the upcoming challenges for the prototype. For instance, to reach higher buffer-gas pressures inside the trap, the aperture sizes of the endcaps can be adapted. Furthermore, the rise and fall flanks of the digital RF waveform can be improved by using advanced high-frequency switches.

Author statement. F.S.: conceptualization, measurements (Greifswald, European XFEL) investigation, formal analysis, writing-original draft, writing: review & editing. T.D.: measurements (European XFEL), writing: review & editing. P.F.: conceptualization, writing — review & editing. A.K.: measurements (European XFEL), writing: review & editing. T.K.: measurements (European XFEL), writing: review & editing. K.L.: resources, writing: review & editing. C.U.: MS SPIDOC project administration, funding acquisition, resources, writing: review & editing. L.S.: conceptualization, funding acquisition, writing: review & editing.

Author declaration. The authors declare that they have no known competing financial interests or personal relationships that could have appeared to influence the work reported in this paper.

Acknowledgments

This work is supported by the European Commission within the Horizon 2020 program (grant agreement ID: 801406). We thank the other members of the MS SPIDOC consortium for many fruitful discussions. In particular, thanks go to Steffi Bandelow, Gerrit Marx, Joachim Schulz, and Yinfei Lu for their contribution at the start of the project.

References

[1] C. Uetrecht et al., *Ion mobility mass spectrometry of proteins and proteinassemblies*, *Chem. Soc. Rev.* **39** (2010) 1633.

[2] Y.S. Eisele et al., *Targeting protein aggregation for the treatment of degenerative diseases*, *Nat. Rev. Drug Discov.* **14** (2015) 759.

[3] H. Madhav and N. Hoda, *An insight into the recent development of the clinical candidates for the treatment of malaria and their target proteins*, *Eur. J. Med. Chem.* **210** (2021) 112955.

[4] *Mass Spectrometry for Single Particle Imaging of Dipole Oriented protein Complexes*, https://www.ms-spidoc.eu/ [accessed: 2023-06-20].

[5] T. Mandl et al., *Structural Heterogeneity in Single Particle Imaging Using X-ray Lasers*, *J. Phys. Chem. Lett.* **11** (2020) 6077.

[6] A. Kádek, K. Lorenzen and C. Uetrecht, *In a flash of light: X-ray free electron lasers meet native mass spectrometry*, *Drug Discov. Today Technol.* **39** (2021) 89.

[7] T. Kierspel et al., *Coherent diffractive imaging of proteins and viral capsids: simulating MS SPIDOC*, *Anal. Bioanal. Chem.* **415** (2023) 4209.

[8] M. Altarelli, *XFEL: The European X-Ray Free-Electron Laser. Technical design report*, DESY-06-097 (2006) [`DOI:10.3204/DESY_06-097`].

[9] *Europe turns on bright X-ray source*, *Nature Photon.* **11** (2017) 609.

[10] H. Han et al., *The XBI BioLab for life science experiments at the European XFEL*, *J. Appl. Crystallogr.* **54** (2021) 7.

[11] E.G. Marklund et al., *Controlling Protein Orientation in Vacuum Using Electric Fields*, *J. Phys. Chem. Lett.* **8** (2017) 4540.

[12] A. Sinelnikova et al., *Protein orientation in time-dependent electric fields: orientation before destruction*, *Biophy. J.* **120** (2021) 3709.

[13] F. Simke, P. Fischer, G. Marx and L. Schweikhard, *Simulations of a digital ion filter and a digital ion trap for heavy biomolecules*, *Int. J. Mass Spectrom.* **473** (2022) 116779.

[14] L. Ding et al., *A digital ion trap mass spectrometer coupled with atmospheric pressure ion sources*, *J. Mass Spectrom.* **39** (2004) 471.

[15] J.W. McCabe et al., *Implementing Digital-Waveform Technology for Extended m/z Range Operation on a Native Dual-Quadrupole FT-IM-Orbitrap Mass Spectrometer*, *J. Am. Soc. Mass Spectrom.* **32** (2021) 2812.

[16] S. Bandelow, G. Marx and L. Schweikhard, *The stability diagram of the digital ion trap*, *Int. J. Mass Spectrom.* **336** (2013) 47.

[17] C. Xiong et al., *The development of charge detection-quadrupole ion trap mass spectrometry driven by rectangular and triangular waves*, *Analyst* **137** (2012) 1199.

[18] J.A. Richards, R.M. Huey and J. Hiller, *A new operating mode for the quadrupole mass filter*, *Int. J. Mass Spectrom. Ion Phys.* **12** (1973) 317.

[19] J.A. Richards, *Quadrupole mass filter spectrum control using pulse width modulation*, *Int. J. Mass Spectrom. Ion Phys.* **24** (1977) 219.

[20] L. Ding, M. Sudakov and S. Kumashiro, *A simulation study of the digital ion trap mass spectrometer*, *Int. J. Mass Spectrom.* **221** (2002) 117.

[21] M. Sudakov and E. Nikolaev, *Ion Motion Stability Diagram for Distorted Square Waveform Trapping Voltage*, *Eur. J. Mass Spectrom.* **8** (2002) 191.

[22] S. Wang and M.V. Johnston, *Airborne nanoparticle characterization with a digital ion trap-reflectron time of flight mass spectrometer*, *Int. J. Mass Spectrom.* **258** (2006) 50.

[23] F.L. Brancia et al., *Digital asymmetric waveform isolation (DAWI) in a digital linear ion trap*, *J. Am. Soc. Mass Spectrom.* **21** (2010) 1530.

[24] H. Koizumi et al., *A novel phase-coherent programmable clock for high-precision arbitrary waveform generation applied to digital ion trap mass spectrometry*, *Int. J. Mass Spectrom.* **292** (2010) 23.

[25] T. Brunner et al., *TITAN's Digital RFQ Ion Beam Cooler and Buncher, Operation and Performance*, *Nucl. Instrum. Meth. A* **676** (2012) 32 [`arXiv:1107.2187`].

[26] L. Li et al., *Portable Digital Linear Ion Trap Mass Spectrometer Based on Separate-Region Corona Discharge Ionization Source for On-Site Rapid Detection of Illegal Drugs*, *Molecules* **27** (2022) 3506.

[27] D. Papanastasiou et al., *The Omnitrap Platform: A Versatile Segmented Linear Ion Trap for Multidimensional Multiple-Stage Tandem Mass Spectrometry*, *J. Am. Soc. Mass Spectrom.* **33** (2022) 1990.

[28] L.A. Pipes, *Matrix Solution of Equations of the Mathieu-Hill Type*, *J. Appl. Phys.* **24** (1953) 902.

[29] G.F. Brabeck and P.T.A. Reilly, *Mapping ion stability in digitally driven ion traps and guides*, *Int. J. Mass Spectrom.* **364** (2014) 1.

[30] D. Beck et al., *A New control system for ISOLTRAP*, *Nucl. Instrum. Meth. A* **527** (2004) 567.

[31] L. Konermann, E. Ahadi, A.D. Rodriguez and S. Vahidi, *Unraveling the Mechanism of Electrospray Ionization*, *Anal. Chem.* **85** (2012) 2.

[32] L. Konermann, H. Metwally, Q. Duez and I. Peters, *Charging and supercharging of proteins for mass spectrometry: recent insights into the mechanisms of electrospray ionization*, *Analyst* **144** (2019) 6157.

[33] M. Yamashita and J.B. Fenn, *Electrospray ion source. Another variation on the free-jet theme*, *J. Phys. Chem.* **88** (1984) 4451.

[34] M.L. Alexandrov et al., *Extraction of ions from solutions under atmospheric pressure as a method for mass spectrometric analysis of bioorganic compounds*, *Rapid Commun. Mass Spectrom.* **22** (2008) 267.

[35] D. Papanastasiou et al., *Experimental and numerical investigations of under-expanded gas flows for optimal operation of a novel multipole differential ion mobility filter in the first vacuum-stage of a mass spectrometer*, *Int. J. Mass Spectrometry* **465** (2021) 116605.

[36] M. Wilm and M. Mann, *Analytical Properties of the Nanoelectrospray Ion Source*, *Anal. Chem.* **68** (1996) 1.

[37] H. Hernández and C.V. Robinson, *Determining the stoichiometry and interactions of macromolecular assemblies from mass spectrometry*, *Nat. Protoc.* **2** (2007) 715.

[38] B. Krichel et al., *Hallmarks of Alpha- and Betacoronavirus non-structural protein 7+8 complexes*, *Sci. Adv.* **7** (2021) eabf1004.

[39] R.H.H. van den Heuvel et al., *Improving the Performance of a Quadrupole Time-of-Flight Instrument for Macromolecular Mass Spectrometry*, *Anal. Chem.* **78** (2006) 7473.

[40] I. Campuzano and K. Giles, *Nanospray Ion Mobility Mass Spectrometry of Selected High Mass Species*, in *Nanoproteomics: Methods in Molecular Biology*, S.A. Toms and R.J. Weil eds., Totowa, NJ, Humana Press (2011), p. 57–70 [`DOI:10.1007/978-1-61779-319-6_5`].

[41] D.A. Dahl, *simion for the personal computer in reflection*, *Int. J. Mass Spectrom.* **200** (2000) 3.

[42] X. Zheng, R.T. Kurulugama, A. Laganowsky and D.H. Russell, *Collision-Induced Unfolding Studies of Proteins and Protein Complexes using Drift Tube Ion Mobility-Mass Spectrometer*, *Anal. Chem.* **92** (2020) 7218.

[43] N.B. Borotto, K.E. Osho, T.K. Richards and K.A. Graham, *Collision-Induced Unfolding of Native-like Protein Ions Within a Trapped Ion Mobility Spectrometry Device*, *J. Am. Soc. Mass Spectrom.* **33** (2021) 83.